

New Monte Carlo method for planar Poisson-Voronoi cells

H. J. Hilhorst

Laboratoire de Physique Théorique*, Bâtiment 210, Université de Paris-Sud
91405 Orsay Cedex, France

February 4, 2008

Abstract

By a new Monte Carlo algorithm we evaluate the sidedness probability p_n of a planar Poisson-Voronoi cell in the range $3 \leq n \leq 1600$. The algorithm is developed on the basis of earlier theoretical work; it exploits, in particular, the known asymptotic behavior of p_n as $n \rightarrow \infty$. Our p_n values all have between four and six significant digits. Accurate n dependent averages, second moments, and variances are obtained for the cell area and the cell perimeter. The numerical large n behavior of these quantities is analyzed in terms of asymptotic power series in n^{-1} . Snapshots are shown of typical occurrences of extremely rare events implicating cells of up to $n = 1600$ sides embedded in an ordinary Poisson-Voronoi diagram. We reveal and discuss the characteristic features of such many-sided cells and their immediate environment. Their relevance for observable properties is stressed.

Keywords: planar Voronoi cells, Monte Calo algorithm, large sidedness

1 Introduction

A Voronoi diagram partitions space into convex cells constructed around a set of point-like ‘seeds’ or ‘particles’, in such a way that each point of space is in the cell of the particle to which it is closest. When the particles are distributed randomly and uniformly, the partitioning is called a Poisson-Voronoi diagram or a Random Voronoi Froth.

Voronoi cells play a role throughout science and engineering and are also of interest to mathematicians. Applications include cellular structures that either arise spontaneously in nature (*e.g.* in biological cellular structures, in soap froths, or in granular materials) or are employed as a tool of analysis (*e.g.* to identify lattice defects in simulations of melting crystals). Many references are given in Ref. [1] and in the encyclopedic monograph on tessellations by Okabe *et al.* [2].

The simplest Voronoi diagrams are of the Poisson type. It is important, therefore, that the properties of Poisson-Voronoi diagrams be understood as well as possible. Here we pursue, by means of a new Monte Carlo method, earlier investigations [1, 3, 4] on such diagrams in the Euclidean plane \mathbb{R}^2 .

The most prominent statistical property of the planar Poisson-Voronoi cell is its ‘sidedness’. We denote by p_n the probability that a cell is n -sided, for arbitrary integer $n \geq 3$. Other properties of interest include the average area of an n -sided cell and the average length of its perimeter; the statistics of the angles at the vertices; and correlations between neighboring cells. All these properties may be expressed as multiple integrals on the particle positions [5, 2], but only a few of them can be calculated explicitly. In particular, no simple closed form expression for p_n is known. An exact relation derived from Euler’s theorem ensures that the average sidedness $\bar{n} \equiv \sum_{n=3}^{\infty} np_n$ is equal to $\bar{n} = 6$.

It is known numerically that p_n peaks at $n = 6$ and falls off rapidly for large n . Hayen and Quine [6] have numerically evaluated the integral for p_3 with high accuracy. For $n = 4, 5, \dots$ the values of p_n stem only from Monte Carlo work. The most accurate reported values of p_n are due to Calka [7] for $4 \leq n \leq 7$ and to Brakke [8] for $8 \leq n \leq 16$. One has $p_{16} \approx 10^{-8}$ and the largest sidedness observed in simulations by conventional algorithms is around $n = 16$. Drouffe and Itzykson [9, 10], as part of an effort to construct field theories on random lattices, developed an improved algorithm by which they estimated p_n for n up to 50. Their results, however, have error bars that for $n \gtrsim 30$ become of the same order as the p_n themselves. Hence simulating many-sided Voronoi cells has remained a challenge.

The interest of investigating Voronoi cells for asymptotically large n was stressed by Le Caër and Delannay [11]. Analytic knowledge of the large

n behavior of p_n , apart from the insight that it provides, also constrains the laws that describe the finite n behavior as observed in experiments and simulations. An example of this interplay between the regimes of finite and of asymptotic n is the theoretical explanation given in Ref. [4] of the failure of Aboav's law [12] for Poisson-Voronoi diagrams.

The analytic study of p_n in the limit $n \rightarrow \infty$ was taken up in Refs. [3] and [1]. It was shown there, among many other things, that asymptotically

$$p_n \simeq C p_n^{(0)}, \quad n \rightarrow \infty, \quad (1.1)$$

with $C = 0.344\,347\dots$ [13] and

$$p_n^{(0)} = \frac{1}{4\pi^2} \frac{(8\pi^2)^n}{(2n)!}. \quad (1.2)$$

In the present work we exploit this asymptotic knowledge. Going beyond Eq. (1.1) we write an equality that is exact for all n rather than merely asymptotic, namely

$$p_n = C_n p_n^{(0)}, \quad (1.3)$$

whence necessarily $\lim_{n \rightarrow \infty} C_n = C$. In this work we focus on C_n and show that it can be expressed as an average

$$C_n = \langle \Theta e^{-\mathbb{V}} \rangle, \quad (1.4)$$

where \mathbb{V} is a known expression in the angular variables that describe the n -sided cell, and Θ is an indicator (*i.e.*, equal to 0 or to 1) imposing a geometric constraint on the set of angles. We will determine the prefactor C_n in (1.3) by Monte Carlo evaluation of the right hand side of Eq. (1.4) for finite $n = 3, 4, \dots$. The Monte Carlo algorithm is new for this problem. Whereas all previously used methods become rapidly inefficient with increasing n , the performance of the algorithm presented here is, very roughly, independent of n . This makes it possible, in particular, to explore the structure of Voronoi cells in the hitherto inaccessible large- n regime.

The remaining sections of this paper are the following. In Sec. 2 the algorithm is described. In Sec. 3 results are presented and discussed for the sidedness probability p_n as well as for the averages and second moments of the cell perimeter and cell area. The asymptotic large- n behavior of these quantities is analyzed numerically. In Sec. 4 we present and discuss characteristic pictures of many-sided Voronoi cells in an environment of ordinary cells. In Sec. 5 we summarize our results.

The algorithm requires the explicit expressions for \mathbb{V} and Θ in Eq. (1.4). Finding these is a matter of considerable technical complexity; it is based on results of Ref. [1] and is the subject of Appendices A and B.

2 Monte Carlo algorithm

2.1 Context

Monte Carlo methods for generating Voronoi cells of Poisson distributed particles are discussed in the monograph by Okabe *et al.* [2]. One class of methods simply determines p_n as the relative frequency of occurrence of n -sided cells. But since p_n decreases to zero faster than exponentially for $n \gtrsim 12$, the statistical precision goes down accordingly. With such methods it is hardly possible to accumulate sufficient statistics for even single-digit precision as soon as $n \approx 16$.

Another class of methods generates cells for a value of n fixed in advance. The first to have done so seem to have been Drouffe and Itzykson [9]. The method employed by Calka [7] is also in this class. These methods face the problem of attrition: a Monte Carlo generated geometrical object, in order to represent a valid n -sided cell, must satisfy certain geometrical constraints. The probability that an attempted generation satisfy the constraints again decreases rapidly with growing n .

The present algorithm, which also fixes n in advance, completely solves the problem of attrition: the geometric constraints are satisfied with a probability that tends to unity when $n \rightarrow \infty$. In order to arrange things this way, a certain amount of rather technical rewriting of the initial problem is necessary. We have confined this rewriting to the Appendices. If one accepts its results, the method is easy to apply.

2.2 Angular variables

An n -sided Voronoi cell around a particle in the origin, as shown in Fig. 1, is specified completely by its n vertex vectors $\mathbf{S}_1, \mathbf{S}_2, \dots, \mathbf{S}_n$. It may be specified alternatively by its n mid-point vectors, *i.e.* the projections $\mathbf{R}_1, \mathbf{R}_2, \dots, \mathbf{R}_n$ of the origin onto the sides. The explicit expression [9, 14, 7, 1] for p_n as a multiple integral on the \mathbf{R}_m is given in Appendix A. It has not, however, been possible to evaluate this integral analytically. By choosing other sets of variables of integration one may recast the original integral in numerous different forms, none of which is simple. For our purpose it is essential to use the angular variables that we will define now.

Let Φ_m and Ψ_m be the polar angles of \mathbf{R}_m and \mathbf{S}_m , respectively. Other angles relevant for this problem are defined in Fig. 1. The $\eta_m = \Psi_{m+1} - \Psi_m$ are the angles between two consecutive vertex vectors and the $\xi_m = \Phi_m - \Phi_{m-1}$ those between two consecutive vertex vectors; n -periodicity in the index m is understood. For fixed sets $\xi = \{\xi_m\}$ and $\eta = \{\eta_m\}$ one may still jointly rotate the set of vertex vectors with respect to the set of mid-point vectors: this modifies only the relative angles β_m and γ_m between the two sets. We

may select any one of these relative angles and call it ‘the’ angle of rotation, since it will determine all others; we will select β_1 . When for a generic β_1 we draw the cell boundary by clockwise constructing its successive segments, then after a turn of 2π it appears not close onto itself but to spiral. A ‘no-spiral condition’ must therefore determine the appropriate value of the angle of rotation β_1 for which the cell boundary closes and which we will denote by $\beta_1 = \beta_*(\xi, \eta)$. This condition reads

$$G(\xi, \eta; \beta_*) = 0 \quad (2.1)$$

where

$$e^{2\pi G} = \prod_{m=1}^n \frac{\cos \gamma_m}{\cos \beta_m}. \quad (2.2)$$

One may note that Eq. (2.2) involves the β_m and γ_m that are themselves determined by the solution $\beta_1 = \beta_*$ of (2.1). For an arbitrary pair (ξ, η) there need not exist a solution to Eq. (2.1). In Appendix B we show that it has a solution, which moreover is unique, if and only if

$$\max_{1 \leq m \leq n} \left[\sum_{\ell=1}^{m-1} (\xi_\ell - \eta_\ell) + \xi_m \right] - \min_{1 \leq m \leq n} \left[\sum_{\ell=1}^{m-1} (\xi_\ell - \eta_\ell) \right] < \pi, \quad (2.3)$$

which is a criterion expressed entirely in terms of the supposedly given sets ξ and η .

After these preliminaries we return to (1.4). The symbol Θ in that expression denotes the indicator function of the domain in (ξ, η) space where (2.3) is satisfied. Finally, the ‘interaction’ \mathbb{V} in (1.4) is given explicitly in terms of the angular variables in Appendix A through a sequence of definitions, Eqs. (A.10) and (A.5)-(A.8), that we will not display here.

2.3 Algorithm for determining p_n

The sidedness probability p_n is given by Eqs. (1.2)-(1.4). We determine it numerically by evaluating $\langle \Theta e^{-\mathbb{V}} \rangle$ as follows. We fix the sidedness n , after which the simulation proceeds as follows.

(i) We draw $n - 1$ random numbers uniformly distributed on $[0, 1]$ and order them. After multiplication by 2π this gives [15] $0 < \bar{\Psi}_1 < \bar{\Psi}_2 < \dots < \bar{\Psi}_{n-1} < 2\pi$. We set $\bar{\Psi}_n = 2\pi$ and choose

$$\begin{aligned} \eta_m &= \bar{\Psi}_{m+1} - \bar{\Psi}_m, & m = 1, \dots, n-1, \\ \eta_n &= \bar{\Psi}_1. \end{aligned} \quad (2.4)$$

We next draw $2n - 1$ random numbers, order them, and discard those of odd rank so that only $n - 1$ are left. After multiplication by 2π this gives

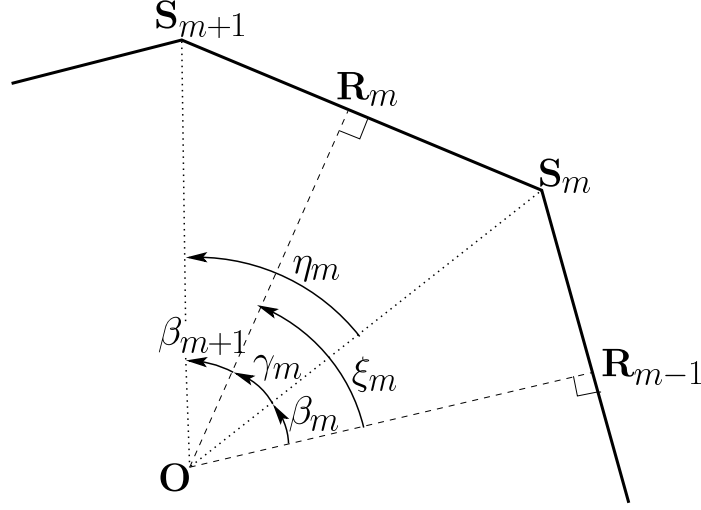


Figure 1: Heavy line: the perimeter of the Voronoi cell around a particle in the origin \mathbf{O} . Dashed and dotted lines connect the origin to the midpoints \mathbf{R}_m and vertices \mathbf{S}_m , respectively. The particles of the neighboring cells are located at $2\mathbf{R}_1, \dots, 2\mathbf{R}_n$. Right angles have been marked. The figure defines the sets of angles ξ_m , η_m , β_m , and γ_m .

$0 < \bar{\Phi}_1 < \bar{\Phi}_2 < \dots < \bar{\Phi}_{n-1} < 2\pi$. We set $\bar{\Phi}_0 = 0$ and choose

$$\begin{aligned}\xi_m &= \bar{\Phi}_m - \bar{\Phi}_{m-1}, & m = 1, \dots, n-1, \\ \xi_n &= 2\pi - \bar{\Phi}_{n-1}.\end{aligned}\tag{2.5}$$

(ii) We check if the pair of sets (ξ, η) thus obtained satisfies Eq. (2.3). If so, then we know that there exists a $\beta_*(\xi, \eta)$ which may be determined from Eq. (2.1), hence $\Theta = 1$ and we proceed with (iii). If not, then it is impossible to satisfy Eq. (2.1), we have $\Theta = 0$, and the attempt to generate an n -sided cell fails. We increase the attempt counter by one unit and return to (i).

(iii) We solve $\beta_*(\xi, \eta)$ from Eq. (2.1) by a numerical iteration procedure which also yields the derivative $G'(\xi, \eta; \beta_*)$ needed in the next step.

(iv) We calculate the weight $\exp(-\mathbb{V})$ according to Eqs. (A.10) and (A.5)-(A.8) of Appendix A and add it to the accumulated weight. We increase the attempt counter by one unit and return to (i).

(v) In the end the total accumulated weight is divided by the total number of attempts, including those that failed. The result is an estimate for p_n .

We remark that the successive cells generated by this procedure are all statistically independent.

2.4 Algorithm for n dependent averages

The simulation method described above allows us to study arbitrary cell properties $F(\mathbf{R}_1, \dots, \mathbf{R}_n)$. Writing $\langle F \rangle_n$ for the average of F subject to a given sidedness n we have

$$\langle F \rangle_n = \frac{\langle I_F \Theta e^{-V} \rangle}{\langle \Theta e^{-V} \rangle}. \quad (2.6)$$

Here the numerator, which generalizes (1.4), has an insertion I_F that derives from F by a radial integration. We recall that the average $\langle \dots \rangle$, defined in (A.15), applies to quantities that depend exclusively on the angular variables. To find I_F from F , we let R_{av} denote the average of the R_m . Upon setting $R_m = R_{\text{av}} \rho_m$ we may express the ρ_m entirely in terms of the angular variables (see Appendix A). Then, if F is of dimension d_F , it may be factorized into a radial and an angular part according to

$$F(\mathbf{R}_1, \dots, \mathbf{R}_n) = (R_{\text{av}}^2/4\lambda)^{d_F/2} \hat{F}(\xi, \eta), \quad (2.7)$$

where we show explicitly the areal particle density λ which had heretofore been scaled away [16]. When (2.7) is integrated over the radial scale R_{av} , an extra factor appears as compared to the same operation for p_n and we find

$$I_F = \frac{\Gamma(n + \frac{1}{2}d_F)}{\Gamma(n)} W^{-d_F/2} \hat{F}, \quad (2.8)$$

where Γ denotes the Gamma function and where we abbreviated

$$W = 4\lambda\pi(1 + n^{-1}V) \quad (2.9)$$

with V given by (A.8).

We will limit ourselves to considering the first and second moments of two quantities that are frequently encountered in applications and that have therefore been the subject of much earlier work, *viz.* the cell perimeter P and the cell area A . These are explicitly given by

$$P = R_{\text{av}}(4\lambda)^{-1/2} \hat{F}_1, \quad A = R_{\text{av}}^2(4\lambda)^{-1} \hat{F}_2, \quad (2.10)$$

with the angular factors

$$\hat{F}_k = \frac{1}{k} \sum_{m=1}^n \rho_m^k (\tan \gamma_m + \tan \beta_{m+1}), \quad k = 1, 2. \quad (2.11)$$

Setting successively $F = P, P^2, A, A^2$ we find that the corresponding insertions in the numerator of Eq. (2.6) are

$$\begin{aligned} I_P &= [\Gamma(n + \frac{1}{2})/\Gamma(n)] W^{-1/2} \hat{F}_1, \\ I_{P^2} &= n W^{-1} \hat{F}_1^2, \\ I_A &= \frac{1}{2} n W^{-1} \hat{F}_2, \\ I_{A^2} &= \frac{1}{4} n(n+1) W^{-2} \hat{F}_2^2. \end{aligned} \quad (2.12)$$

The simulation steps for finding the numerator of Eq. (2.6) are the same as for p_n except that (iv) and (v) are replaced with (iv') and (v') given below.

(iv') We multiply the insertion I_F of the quantity F of interest by the weight $\exp(-\mathbb{V})$ and accumulate the value thus obtained.

(v') In the end the total accumulated value is divided by the total number of attempts and by the estimate obtained for p_n . This provides an estimate for $\langle F \rangle_n$. The numerical data shown will all be for $\lambda = 1$.

3 Results and discussion

3.1 The distribution of \mathbb{V} and the indicator Θ

Before discussing our results for the sidedness probability p_n we briefly consider the quantities \mathbb{V} and Θ that via (1.3) and (1.4) enter into its definition. Let $P(\mathbb{V})$ denote the probability distribution of \mathbb{V} and $\phi_n \equiv \langle \Theta \rangle$ the probability for an attempted cell generation to be successful. In terms of these we may rewrite (1.4) as

$$C_n = \phi_n \int d\mathbb{V} P(\mathbb{V}) e^{-\mathbb{V}}, \quad (3.1)$$

which exhibits the important intermediate role of $P(\mathbb{V})$ and ϕ_n .

In order to show what $P(\mathbb{V})$ looks like, we have plotted its logarithm in Fig. 2 for $n = 50, 100, 200$, and 400 . The curves clearly demonstrate that for $n \rightarrow \infty$ there is convergence to a limit. For $\mathbb{V} \rightarrow \pm\infty$ the limit distribution appears to decay exponentially, $P(\mathbb{V}) \sim \exp(-\kappa_{\pm}|\mathbb{V}|)$, but with very different decay constants: we obtain $\kappa_+ = 0.185 \pm 0.05$ from a fit in the range $3 \leq \mathbb{V} \leq 30$ followed by extrapolation to $n = \infty$, and $\kappa_- = 2.47 \pm 0.02$ from a fit in the range $-3 \leq \mathbb{V} \leq -1.5$. This large \mathbb{V} behavior has not yet been explained theoretically.

The Θ function in (1.4) imposes constraint (2.3) and is at the origin of the failed generation attempts. Whereas these do not contribute to p_n in step (iv) of the algorithm above, Eq. (3.1) shows that via $\langle \Theta \rangle = \phi_n$ they do enter into the determination of its normalization. In the last column of Table 1 we list the fractions ϕ_n of successful attempts as determined from the simulation. Although ϕ_n is equal only to $\phi_3 = 0.058$ for $n = 3$, it turns out to rise rapidly with n , is already as high as $p_{10} = 0.8$ for $n = 10$, and tends to unity for $n \rightarrow \infty$. That is, attrition disappears in the large n limit.

This brings out the two key steps that are responsible for the success of the present algorithm: (i) the limit distribution of $P(\mathbb{V})$ has become n independent since we extracted from the initial expression for p_n the appropriate n dependent prefactor $p_n^{(0)}$ given in (1.2); and (ii) attrition disappears for

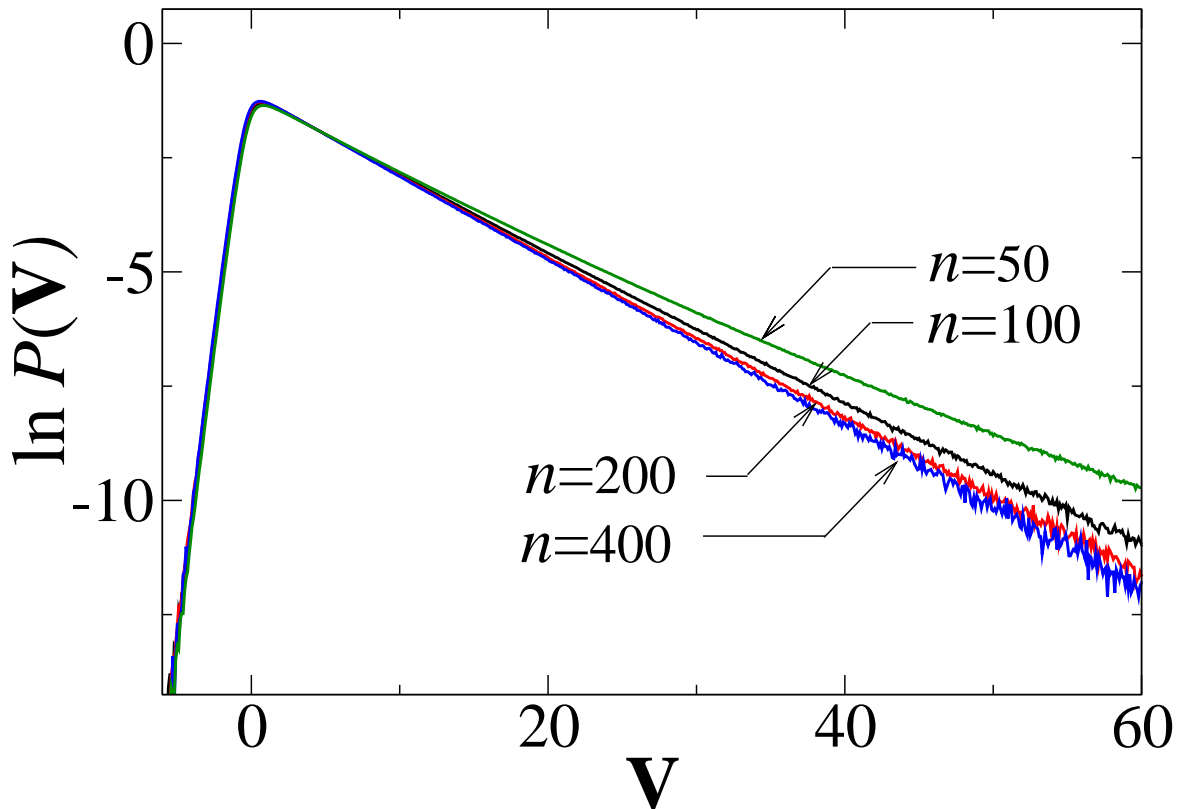


Figure 2: Logarithm of the probability distribution $P(\mathbb{V})$ of \mathbb{V} [see Eq. (3.1)] for four different values of n , showing convergence to a limit distribution for $n = \infty$.

large n because of our choice of the angles (ξ, η) as the variables of integration.

3.2 Sidedness probability p_n

In Table 1 we present the results for the sidedness probability p_n for n in the range between $n = 3$ and $n = 1600$. They are based on a number N_n of generation attempts given in the fourth column of that table.

The second column of Table 1 shows the best results for p_n found in the literature for each value of n . The p_3 value was obtained by numerical integration, the other p_n are Monte Carlo results. For p_4, \dots, p_7 the statistical error is in the last decimal; for higher n the standard deviations are indicated.

Our own results for p_n , given in the third column of Table 1, are accurate up to absolute errors of order less than 10^{-5} . Standard deviations were calculated by subdividing the data into twenty or more groups and considering the dispersion of the group averages. We will now discuss these results as a function of n .

Case $n = 3$. – The probability p_3 for a cell to be three-sided is the only one that has been evaluated by numerical integration. This was done by Hayen and Quine [6], who reduced the original integral to a four-dimensional one. They present a 12-digit result of which the second column of Table 1 shows only the first seven significant decimals. For $n = 3$ we performed an especially long run with the purpose of testing our Monte Carlo method and checking the result of Ref. [6]. As shown in Table 1, our method reproduces six significant digits of Hayen and Quine’s result and leaves their value within our error bars.

For all $n > 3$ the literature results are based on Monte Carlo evaluation.

Cases $n = 4$ through $n = 7$. – The most accurate literature results in this intermediate regime are due to Calka [7], whose algorithm like ours fixed n in advance. Our results are fully compatible with those of Ref. [7].

Cases $n = 8$ through $n = 15$. – Monte Carlo results obtained in the 1980’s by Brakke [8] for $3 \leq n \leq 16$ stayed for a long while the most accurate ones that were available. Our simulations confirm all of Brakke’s results. Beyond $n \approx 10$ the accuracy of the Monte Carlo algorithm of Ref. [8] rapidly goes down with increasing n , and for $n = 16$ its error bars are as large as the result itself. This effect is simply due to the low relative frequency of cells of so many sides, the number n not being fixed in this method. By contrast, the accuracy of our method, for a fixed amount of computer time invested per value of n , stays roughly constant.

Case $n \geq 16$. – Drouffe and Itzykson [9] developed a more powerful simulation method aimed at simulating cells of larger sidedness. In their method n is again fixed in advance. Their accuracy amounts to roughly a single significant digit in the regime $16 \leq n \lesssim 25$; for $n \gtrsim 25$ the error becomes again of the order of p_n itself. This error increase is due to attrition, *i.e.*, an increasing rejection rate of configurations that are generated but do not satisfy the required geometrical constraints. From our data it appears that for $n \gtrsim 25$ the work of Ref. [9] misses the true values by an ever larger factor and that only their logarithmic order of magnitude is right [17]. Again, the method of the present work maintains an error in the fifth digit, *i.e.*, a relative error not larger than 10^{-4} .

Case of extremely large n . – The range of n from 50 to 1600 had so far been unexplored territory. In this very large n regime attrition is negligible and, for a constant calculational effort per value of n , the method keeps producing results with an error only in the fourth significant digit. The probabilities p_n are extremely small. Numerically we could easily handle such small numbers by first factorizing out $p_n^{(0)}$ of which we computed and stored only the logarithm. As discussed in subsection 3.1, the remaining factor $C_n = \langle \Theta e^{-V} \rangle$ has a finite distribution and hence causes no underflow problems.

Generating the values of such ‘unphysically’ small probabilities is much

more than a mere technical achievement. First, it provides another check that the program works correctly; indeed we find that for $n \rightarrow \infty$ the ratio $p_n/Cp_n^{(0)} = C_n/C$ tends to unity as it should. Second, it gives access to the large n expansion of p_n to be discussed in subsection 3.3. Thirdly and most importantly, values of n this large are required to see the separation of length scales that occurs in the many-sided cell; this is the subject of section 4.

Sum rules. – The p_n should obey certain sum rules. Upon summing the p_n of Table 1 and writing $\overline{X_n} = \sum_{n=3}^{\infty} X_n p_n$ we find

$$\begin{aligned} \sum_{n=3}^{\infty} p_n &= 1.000\,010(15), \\ \overline{n} &= 6.000\,1(1), \\ \overline{n^2} &= 37.781\,6(7), \\ \mu \equiv \overline{n^2} - \overline{n}^2 &= 1.780\,4, \end{aligned} \tag{3.2}$$

with an error in μ at most equal to ± 0.0015 but probably smaller due to partial cancellation of the errors in $\overline{n^2}$ and \overline{n}^2 . The first and second relations of (3.2) may be compared to the exactly known values 1 and 6, respectively. The second moment $\overline{n^2}$ has an exact expression as a double integral [18], which when evaluated numerically gives $\overline{n^2} = 37.780\,811\dots$. Hence $\mu = 1.780\,811\dots$ numerically exactly. We therefore see that, when their error bars are taken into account, our Monte Carlo data are in excellent agreement with these sum rules.

Conclusion. – The general conclusion of this subsection is that for low n (say $n \lesssim 8$) our method is probably as good as several of the existing ones. If we did slightly outperform them in that small n regime, that was only because of the length of our runs. However, for larger N (say $n \gtrsim 8$) our method has a decisive advantage over the existing ones.

3.3 Asymptotic behavior of p_n

On the basis of the numerical data we will now discuss the asymptotic behavior of p_n for $n \rightarrow \infty$. Analytically it is known that $p_n = C_n p_n^{(0)}$ with $p_n^{(0)}$ given by Eq. (1.2) and where the correction factor C_n may be obtained by a series expansion that classifies contributions according to their power in $n^{-1/2}$. On that basis Ref. [3] fitted the limited p_n data available at that time (essentially $n \lesssim 30$) by a correction term proportional to $n^{-1/2}$. It remained possible, however, that the coefficient of the $n^{-1/2}$ term would cancel, and indeed Drouffe and Itzykson [9] had hypothesized earlier that the leading correction was of order n^{-1} .

The numerical data of this work now indicate unambiguously that the

series is actually one in powers of n^{-1} ,

$$p_n = \frac{C}{4\pi^2} \frac{(8\pi^2)^n}{(2n)!} \left[1 - \frac{e_1}{n} + \frac{e_2}{n^2} - \frac{e_3}{n^3} + \dots \right], \quad (3.3)$$

where e_1, e_2, \dots , are numerical coefficients.

The factor in square brackets in Eq. (3.3) is equal to C_n/C , which for $n \rightarrow \infty$ is known to tend to unity. In Fig. 3, in order to find the corrections to the leading order term in (3.3), we have plotted $n(1 - C_n/C) = e_1 - e_2n^{-1} + \dots$ against n^{-1} . This figure shows that the intercept with the vertical axis is located at $e_1 = 14.00 \pm 0.05$. We may now proceed by subtracting this estimated value of e_1 from the curve of Fig. 3, multiply it again by n , and look for a new intercept with the vertical axis which, if it is well-defined, is equal to $-e_2$. Upon iterating until the statistical errors obscure a well-defined intercept we obtained in this way estimates for the first few e_i . The uncertainties increase with the index i . We found

$$e_1 = 14.00 \pm 0.05, \quad e_2 = 94 \pm 4, \quad e_3 = 375 \pm 80, \quad (3.4)$$

in which the errors are correlated: the values deviate together upward or downward. The important conclusion is that p_n has a series expansion in powers of n^{-1} . The cancellation of the half-integer powers in the expansion of Ref. [1] is no doubt due to a symmetry in the theory that still remains to be identified.

In a final remark we wish to stress that finding this asymptotic expansion is different from finding a ‘best fit’, which we do not attempt here. The curve of Fig. 3 is close to the sum of a constant and an exponential in n^{-1} , but we have no reason to believe that there exists a simple analytical expression that fits all data within their error bars.

3.4 Perimeter and area

We have simulated the two cell properties that have received the greatest attention in the literature, *viz.* the cell perimeter P and the cell area A . We determined the average, the second moment and the variance of both of these quantities as a function of n . The perimeter results are summarized in Table 2 and the area results in Table 3.

Similar tables extracted from the literature were compiled by Okabe *et al.* [2]. However, by far the most accurate ones appear in unpublished work by Brakke [8] and concern the regime $3 \leq n \leq 16$. All our area and perimeter data are compatible with those of Ref. [8], but our error bars are strongly reduced. A further check on the numerical data is provided by two more sum rules,

$$\overline{P_n} = 4.000\,035(65), \quad \overline{A_n} = 1.000\,02(2), \quad (3.5)$$

n	Literature [6]-[9]	This work		
	p_n	p_n	N_n	ϕ_n
3	$1.124001... \times 10^{-2}$	$(1.124000 \pm 0.000021) \times 10^{-2}$	1.2×10^{10}	0.0580
4	1.06838×10^{-1}	$(1.068454 \pm 0.000025) \times 10^{-1}$	2×10^9	0.1730
5	2.5946×10^{-1}	$(2.59444 \pm 0.00007) \times 10^{-1}$	1.6×10^9	0.3077
6	2.9473×10^{-1}	$(2.94723 \pm 0.00009) \times 10^{-1}$	2×10^9	0.4391
7	1.9877×10^{-1}	$(1.98768 \pm 0.00007) \times 10^{-1}$	4×10^8	0.5564
8	$(9.0116 \pm 0.0020) \times 10^{-2}$	$(9.0131 \pm 0.0006) \times 10^{-2}$	10^8	0.6554
9	$(2.9644 \pm 0.0012) \times 10^{-2}$	$(2.9652 \pm 0.0002) \times 10^{-2}$	8×10^7	0.7361
10	$(7.4471 \pm 0.0059) \times 10^{-3}$	$(7.4487 \pm 0.0006) \times 10^{-3}$	8×10^7	0.8002
11	$(1.4796 \pm 0.0026) \times 10^{-3}$	$(1.4818 \pm 0.0002) \times 10^{-3}$	6×10^7	0.8501
12	$(2.409 \pm 0.011) \times 10^{-4}$	$(2.4000 \pm 0.0002) \times 10^{-4}$	6×10^7	0.8884
13	$(3.18 \pm 0.04) \times 10^{-5}$	$(3.2324 \pm 0.0003) \times 10^{-5}$	6×10^7	0.9175
14	$(3.60 \pm 0.13) \times 10^{-6}$	$(3.6835 \pm 0.0004) \times 10^{-6}$	4×10^7	0.9393
15	$(3.7 \pm 0.4) \times 10^{-7}$	$(3.6017 \pm 0.0004) \times 10^{-7}$	4×10^7	0.9556
16	$(2.3 \pm 0.3) \times 10^{-8}$	$(3.0574 \pm 0.0004) \times 10^{-8}$	4×10^7	0.9677
17		$(2.2762 \pm 0.0002) \times 10^{-9}$	4×10^7	0.9765
18	$(1.3 \pm 0.5) \times 10^{-10}$	$(1.4989 \pm 0.0002) \times 10^{-10}$	4×10^7	0.9830
19		$(8.7983 \pm 0.0013) \times 10^{-12}$	4×10^7	0.9878
20	$(1.5 \pm 0.8) \times 10^{-13}$	$(4.6314 \pm 0.0004) \times 10^{-13}$	8×10^7	0.9912
21		$(2.1994 \pm 0.0004) \times 10^{-14}$	2×10^7	0.9937
22		$(9.4835 \pm 0.0017) \times 10^{-16}$	2×10^7	0.9955
23		$(3.7227 \pm 0.0005) \times 10^{-17}$	2×10^7	0.9968
24		$(1.3379 \pm 0.0003) \times 10^{-18}$	2×10^7	0.9977
25	$(9.6 \pm 5.9) \times 10^{-21}$	$(4.4184 \pm 0.0004) \times 10^{-20}$	4×10^7	0.9984
30	$(1.3 \pm 1.1) \times 10^{-29}$	$(5.4595 \pm 0.0005) \times 10^{-28}$	4×10^7	0.9997
40	2.4×10^{-50}	$(6.7349 \pm 0.0006) \times 10^{-46}$	8×10^7	1.0000
50	1.5×10^{-75}	$(5.223 \pm 0.001) \times 10^{-66}$	1.6×10^7	1.0000
60		$(7.192 \pm 0.002) \times 10^{-88}$	1.2×10^7	1.0000
70		$(3.4805 \pm 0.0004) \times 10^{-111}$	3×10^7	1.0000
80		$(9.598 \pm 0.002) \times 10^{-136}$	10^7	1.0000
90		$(2.1616 \pm 0.0005) \times 10^{-161}$	0.8×10^7	1.0000
100		$(5.2691 \pm 0.0006) \times 10^{-188}$	1.6×10^7	1.0000
150		$(1.0535 \pm 0.0002) \times 10^{-332}$	4×10^6	1.0000
200		$(3.818 \pm 0.001) \times 10^{-492}$	4×10^6	1.0000
300		$(1.084 \pm 0.001) \times 10^{-841}$	2×10^6	1.0000
400		$(9.863 \pm 0.003) \times 10^{-1221}$	4×10^6	1.0000
600		$(3.645 \pm 0.002) \times 10^{-2040}$	10^6	1.0000
800		$(1.326 \pm 0.001) \times 10^{-2918}$	2×10^6	1.0000
1000		$(6.365 \pm 0.003) \times 10^{-3841}$	1.6×10^6	1.0000
1200		$(3.262 \pm 0.002) \times 10^{-4798}$	1.2×10^6	1.0000
1400		$(1.385 \pm 0.001) \times 10^{-5784}$	0.8×10^6	1.0000
1600		$(7.4306 \pm 0.0020) \times 10^{-6796}$	4×10^6	1.0000

Table 1: The sidedness probability p_n . Second column: literature data taken from Hayen and Quine [6] for p_3 ; from Calka [7] for p_4, \dots, p_7 ; from Brakke [8] for p_8, \dots, p_{15} ; and from Drouffe and Itzykson [9] for p_n with $n \geq 16$. Third column: p_n and its standard deviation calculated by the Monte Carlo method of this work. Fourth column: number N_n of cell generation attempts. Fifth column: fraction ϕ_n of successful attempts.

n	$\langle P \rangle_n$		$\langle P^2 \rangle_n$		$\langle \delta P^2 \rangle_n^{1/2}$
3	2.740296	(2)	8.17130	(2)	0.81368
4	3.219524	(3)	11.04819	(2)	0.82634
5	3.642658	(3)	13.96626	(3)	0.83504
6	4.026307	(4)	16.91958	(4)	0.84169
7	4.380000	(6)	19.90272	(6)	0.84702
8	4.710196	(8)	22.91084	(8)	0.85140
9	5.020869	(12)	25.94026	(12)	0.85506
10	5.315211	(11)	28.98790	(12)	0.85816
11	5.595488	(10)	32.05043	(12)	0.86078
12	5.863536	(11)	35.12588	(13)	0.86304
13	6.12072	(2)	38.2114	(2)	0.86497
14	6.36824	(1)	41.3055	(2)	0.86664
15	6.60705	(2)	44.4066	(2)	0.86809
16	6.83797	(2)	47.5136	(3)	0.86936
17	7.06173	(2)	50.6258	(2)	0.87047
18	7.27884	(2)	53.7410	(3)	0.87145
19	7.48992	(2)	56.8598	(3)	0.87233
20	7.69544	(1)	59.9820	(3)	0.87310
21	7.89576	(3)	63.1066	(4)	0.87380
22	8.09118	(3)	66.2318	(5)	0.87442
23	8.28215	(2)	69.3596	(3)	0.87499
24	8.46892	(3)	72.4890	(4)	0.87551
25	8.65171	(2)	75.6198	(4)	0.87598
30	9.51379	(2)	91.2825	(5)	0.87783
40	11.03971	(1)	122.6501	(4)	0.88005
50	12.37983	(2)	154.0370	(5)	0.88135
60	13.58887	(3)	185.4355	(7)	0.88219
70	14.69896	(2)	216.8384	(6)	0.88279
80	15.73105	(2)	248.2460	(7)	0.88323
90	16.69951	(3)	279.6545	(8)	0.88357
100	17.61487	(2)	311.0645	(8)	0.88384
150	21.61817	(3)	468.1280	(12)	0.88465
200	24.98833	(3)	625.1998	(11)	0.88505
300	30.63607	(2)	939.3527	(12)	0.88544
400	35.39384	(2)	1253.5092	(13)	0.88564
600	43.37090	(4)	1881.820	(3)	0.88584
800	50.09346	(2)	2510.143	(2)	0.88593
1000	56.01490	(1)	3138.456	(2)	0.88599
1200	61.36764	(1)	3766.773	(2)	0.88603
1400	66.28953	(2)	4395.087	(4)	0.88606
1600	70.87047	(2)	5023.408	(2)	0.88608
∞					0.886226...

Table 2: Estimates of the average $\langle P \rangle_n$, the second moment $\langle P^2 \rangle_n$, and the root-mean-square fluctuation $\langle \delta P^2 \rangle_n^{1/2}$ of the cell perimeter P . The numbers in parentheses represent the standard deviation in the last digit. The entries of the third column have an error of at most one unit in their last digit. The limit value $\frac{1}{2}\pi^{1/2} = 0.886226...$ for $n = \infty$ has the status of a conjecture.

n	$\langle A \rangle_n$	$\langle A^2 \rangle_n$	$n^{-1/2} \langle \delta A^2 \rangle_n^{1/2}$
3	0.343087 (3)	0.161573 (3)	0.12092
4	0.558052 (4)	0.401285 (5)	0.14989
5	0.774080 (4)	0.73675 (1)	0.16586
6	0.995789 (5)	1.17953 (2)	0.17698
7	1.22251 (1)	1.73516 (3)	0.18541
8	1.45328 (1)	2.40724 (3)	0.19200
9	1.68736 (1)	3.19847 (4)	0.19756
10	1.92408 (2)	4.11064 (7)	0.20213
11	2.16295 (2)	5.1451 (1)	0.20599
12	2.40366 (2)	6.3033 (1)	0.20929
13	2.64578 (2)	7.5854 (1)	0.21217
14	2.88906 (3)	8.9920 (1)	0.21469
15	3.13331 (3)	10.5234 (1)	0.21689
16	3.37835 (3)	12.1797 (2)	0.21885
17	3.62416 (2)	13.9619 (2)	0.22059
18	3.87034 (3)	15.8680 (2)	0.22215
19	4.11703 (3)	17.8996 (3)	0.22357
20	4.36415 (3)	20.0570 (3)	0.22484
21	4.61158 (4)	22.3394 (3)	0.22601
22	4.85923 (4)	24.7464 (4)	0.22706
23	5.10715 (4)	27.2790 (4)	0.22803
24	5.35531 (5)	29.9371 (5)	0.22891
25	5.60358 (6)	32.7198 (6)	0.22974
30	6.84686 (6)	48.5090 (6)	0.23306
40	9.33913 (4)	89.470 (1)	0.23723
50	11.83458 (7)	142.932 (2)	0.23977
60	14.33183 (6)	208.900 (2)	0.24146
70	16.82979 (6)	287.363 (3)	0.24267
80	19.3283 (1)	378.331 (4)	0.24358
90	21.82726 (8)	481.800 (4)	0.24429
100	24.32627 (6)	597.763 (3)	0.24485
150	36.8236 (2)	1365.10 (1)	0.24658
200	49.3224 (1)	2444.94 (1)	0.24742
300	74.3214 (2)	5542.16 (3)	0.24826
400	99.3206 (1)	9889.33 (3)	0.24871
600	149.3196 (3)	22333.58 (1)	0.24914
800	199.3201 (2)	39778.23 (6)	0.24935
1000	249.3192 (2)	62222.3 (1)	0.24948
1200	299.3193 (2)	89666.7 (1)	0.24957
1400	349.3187 (3)	122110.8 (2)	0.24963
1600	399.3190 (2)	159555.4 (2)	0.24968
∞			0.250000...

Table 3: Estimates of the average $\langle A \rangle_n$, the second moment $\langle A^2 \rangle_n$, and the normalized root-mean-square fluctuation $n^{-1/2} \langle \delta A^2 \rangle_n^{1/2}$ of the cell area A . The numbers in parentheses represent the standard deviation in the last digit. The entries of the third column have an error of at most one unit in their last digit. The limit value $\frac{1}{4}$ for $n = \infty$ has the status of a conjecture.

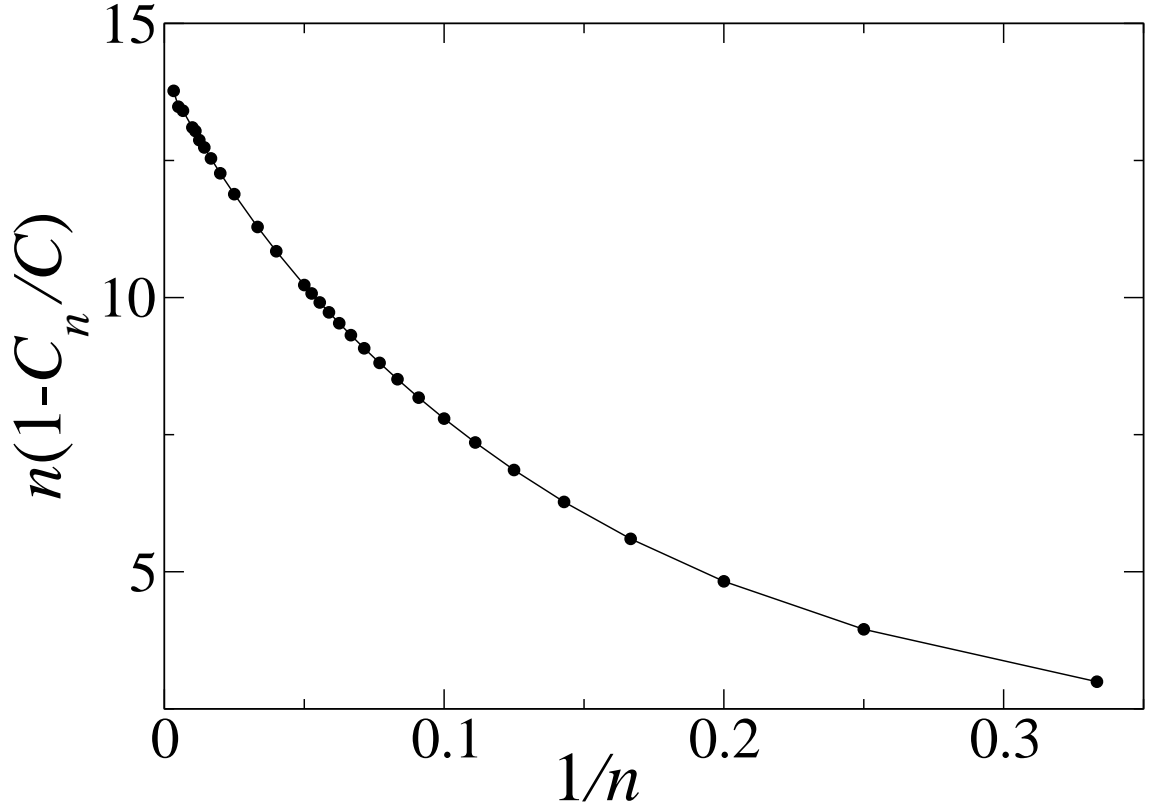


Figure 3: To study the asymptotic large n behavior of the sidedness probability $p_n = C_n p_n^{(0)}$ we plot the quantity $n(1 - C_n/C)$ where $C = \lim_{n \rightarrow \infty} C_n$ [see Eqs. (1.2) and (1.3)]. The solid line connects the data points. Data shown are in the range $3 \leq n \leq 300$. The largest error bars occur for small $1/n$ and are of the order of the data symbols. The intercept of the curve with the vertical axis is the coefficient e_1 of the leading correction term in the expansion of Eq. (3.3).

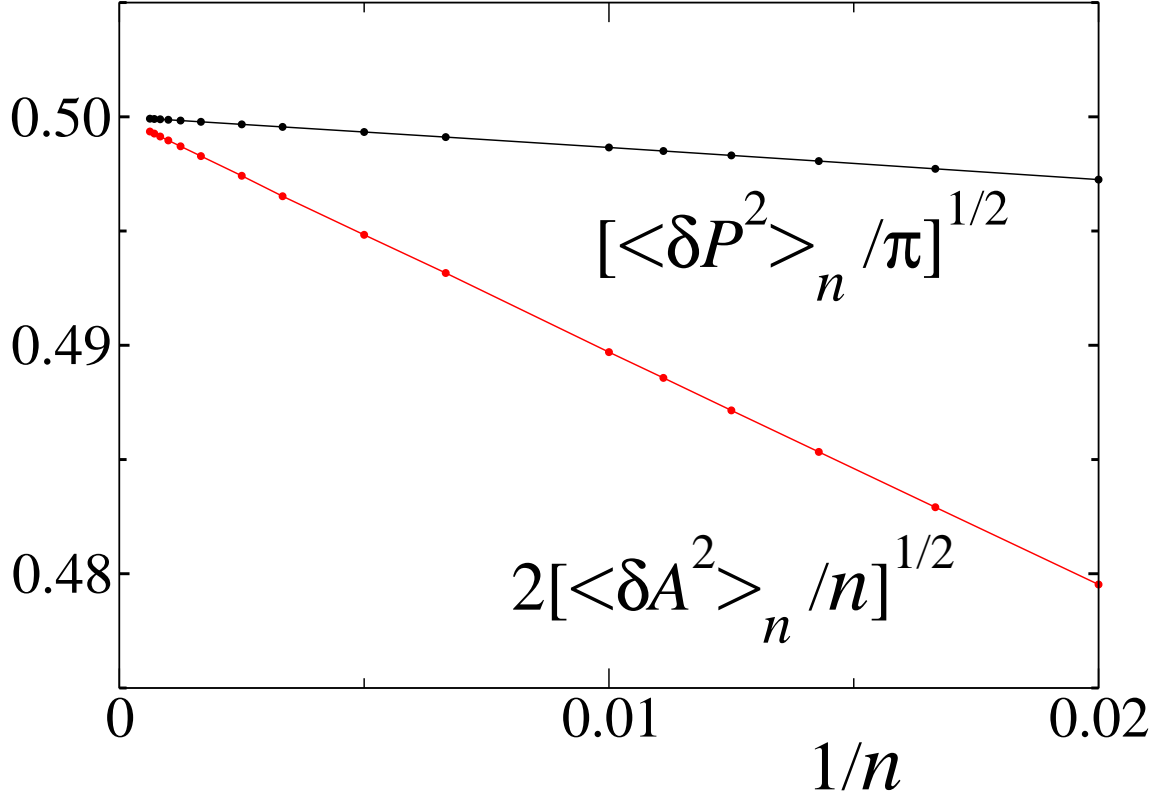


Figure 4: The asymptotic large- n behavior of the root mean square fluctuations $\langle \delta P^2 \rangle_n^{1/2}$ and $\langle \delta A^2 \rangle_n^{1/2}$ of the perimeter and the area, respectively, of the n sided cell. Data shown are in the range $50 \leq n \leq 1600$. The error bars are smaller than the data points. The two curves that connect the data points are asymptotically straight lines which for $n \rightarrow \infty$ both appear to converge $\frac{1}{2}$.

for which the exact values are 4 and 1, respectively.

We now turn to the large n behavior. Our data indicate the expansions

$$\begin{aligned}\langle P \rangle_n &= (\pi n)^{\frac{1}{2}} + a_{\frac{1}{2}} n^{-\frac{1}{2}} + a_{\frac{3}{2}} n^{-\frac{3}{2}} + \dots, \\ \langle P^2 \rangle_n &= \pi n + b_0 + b_1 n^{-1} + \dots, \\ \langle A \rangle_n &= \frac{1}{4}n + c_0 + c_1 n^{-1} + \dots, \\ \langle A^2 \rangle_n &= (\frac{1}{4}n)^2 + d_{-1}n + d_0 + \dots,\end{aligned}\tag{3.6}$$

which again go down by integer powers of n . They imply that the variances have the series

$$\begin{aligned}\langle P^2 \rangle_n - \langle P \rangle_n^2 &= b_0 - 2\pi^{\frac{1}{2}}a_{\frac{1}{2}} + \dots \\ \langle A^2 \rangle_n - \langle A \rangle_n^2 &= (d_{-1} - \frac{1}{2}c_0)n + \dots\end{aligned}\tag{3.7}$$

The leading terms in each of the four series of Eq. (3.6) are known from theoretical analysis [3, 1]. Heuristically they follow from the sole observation that in the large n limit the Voronoi cell becomes a circle of radius $R_c = (n/4\pi)^{1/2}$. Theoretical analysis can in principle also produce the higher order terms in (3.6), but this has not been attempted yet. Consequently, the leading coefficients of the series in (3.7) are not known analytically. Here our simulations results provide answers.

In Fig. 4 we have plotted $[\langle \delta P^2 \rangle_n / \pi]^{1/2}$ and $2[\langle \delta A^2 \rangle_n / n]^{1/2}$. The numerical data strongly point to limit values equal to $\frac{1}{2}$ for both quantities when $n \rightarrow \infty$. Conjecturing that these limits are exact we then conclude that

$$b_0 - 2\pi^{\frac{1}{2}}a_{\frac{1}{2}} = \frac{1}{4}\pi, \quad d_{-1} - \frac{1}{2}c_0 = \frac{1}{16}.\tag{3.8}$$

Analysis of the $\langle P^2 \rangle_n$ data to next order suggests that $\langle P^2 \rangle_n / (\pi n) - 1$ tends to -1 as $n \rightarrow \infty$. Conjecturing that this, too, is exact and combining it with the first one of Eqs. (3.8) we arrive at

$$a_{\frac{1}{2}} = -\frac{5}{8}\pi^{\frac{1}{2}}, \quad b_0 = -\pi,\tag{3.9}$$

We do not attempt, however, a similar analytical conjecture for the second pair of coefficients, c_0 and d_{-1} , nor will we pursue estimates for the higher order coefficients in the series (3.6) and (3.7), except below in connection with Lewis' law.

Lewis' celebrated law [19] is an empirical statement about one of the cell's most conspicuous properties, *viz.* the relation between its area and its number of sides. The law states that the average area $\langle A \rangle_n$ of an n -sided cell increases with n as

$$\langle A \rangle_n = \frac{a_0}{\lambda}(n - n_0),\tag{3.10}$$

where a_0 and n_0 are constants and where we have displayed again the dependence on the areal particle density λ . Sometimes (see the discussion in Ref. [2]) this law is written in the more restricted one-parameter form

$$\langle A \rangle_n = \frac{b(n-6) - 1}{\lambda} \quad (3.11)$$

It is found, however, that $\langle A \rangle_n$ deviates from linearity with n in simulations of Poisson-Voronoi diagrams as well as in the data from most experimental systems. We now look at what the asymptotic analysis has to say.

In Refs. [3, 1] we proved that asymptotically

$$\langle A \rangle_n \simeq \pi R_c^2 = \frac{n}{4\lambda}, \quad n \rightarrow \infty. \quad (3.12)$$

and this result has been incorporated in the series for $\langle A \rangle_n$ in (3.6). A coefficient $a_0 \approx \frac{1}{4}$ had since long been suspected by various authors [9, 20, 21]. Going now beyond (3.12) and proceeding in the same way as for p_n , we can determine the coefficients of the series of (3.6) for $\langle A \rangle_n$ on the basis of our simulation results of Table 2. This yields

$$c_0 = -0.6815(5), \quad c_1 = 0.750(5), \quad c_2 = 3.15(10). \quad (3.13)$$

We now consider the laws (3.10) and (3.11). The fact that we found c_1, c_2, \dots to be nonvanishing confirms once more that $\langle A \rangle_n$ is not strictly linear in n . From the above it follows that in (3.10) one should choose

$$n_0 = -4c_0 = 2.7260(4) \quad (3.14)$$

if one wishes it to correctly represent the asymptotic behavior of $\langle A \rangle_n$ for Poisson-Voronoi cells. This is of course different from finding a best fit to a limited set of $\langle A \rangle_n$ data in a restricted n interval. If that is the purpose, the values of a_0 and n_0 will depend on the available data and on the way the fit is carried out. The one-parameter law (3.11) postulates a relation between a_0 and n_0 that is violated in the asymptotic expansion. Hence (3.11) cannot be used to describe the large n behavior of $\langle A \rangle_n$ and merely has the status of an empirical fit to the data, the value of b again depending on the data set and on how the fit is done.

4 Characteristic cell shapes

It has been established [3, 1] that in the large n limit the Voronoi cell tends to a disk of radius $R_c = (n/4\pi)^{1/2}$ [22]. In Ref. [1] it was furthermore shown that the cell perimeter undergoes ‘elastic’ deformations from circularity, the elasticity being, of course, of entropic origin. The probability law of these

deformations was given in the large n limit. In this section we show how our Monte Carlo method allows us what was hitherto impossible, namely to simulate for any finite n the detailed statistics of the cell shape.

We Monte Carlo generated cells of prescribed sidedness n in a ‘natural’, that is, an unbiased, environment. This was done as follows. For a given n the cell angles (ξ, η) were drawn randomly and β_* was found according to the rules of section 2.3. The cell radius was taken equal to its most probable value $R_c = (n/4\pi)^{1/2}$ and the cell boundary was constructed. This boundary, together with the position of the central particle, fixes the positions of the n first neighbor particles. We then determined the cell’s fundamental domain \mathcal{F} , that is, the union of the n disks of radius S_m centered at the vertices \mathbf{S}_m . The complement of \mathcal{F} in a large rectangle of suitable size was subsequently filled randomly with particles of a uniform density equal to one. The particles added by this procedure are all necessarily second or higher order neighbors of the central one. The Voronoi construction was finally applied to the full collection of particles to complete the Voronoi cell diagram.

4.1 Cells of $n = 24, 48$, and 96 sides

We have generated typical cell shapes for a sequence of values of n , starting with $n = 3$ and doubling n each time. Figs. 5, 6, and 7, in which the dots represent the particles, show the results for cells of $n = 24, 48$, and 96 neighbors. The three pictures are at different scales but all have unit particle density. This picture sequence illustrates the tendencies that characterize many-sided cells. One tendency is for the first neighbor cells to be elongated. This feature is apparent already for $n = 24$ and becomes very pronounced for $n = 48$, whereas the $n = 96$ cell has *only* very elongated neighbors. The same phenomenon was observed by Lauritsen *et al.* [21], but in a different system. These authors consider Poisson-Voronoi diagrams to which they assign an ‘energy’ that favors many-sided cells. Snapshots of their configurations show a dense structure of many-sided cells (of sidednesses higher than $n = 60$) separated by mostly four-sided elongated cells. Their procedure does not, however, provide estimates for p_n in an unbiased Poisson-Voronoi diagram.

Another tendency, appearing similarly in Ref. [21], is for the first-neighbor particles to align on what tends towards a continuous curve. Whereas for $n = 24$ some imagination is still needed to see this curve, it becomes clearly distinguishable for $n = 48$ and is immediately obvious to the eye for $n = 96$. The typical distance between nearest neighbor particles along this curve decreases as $2\pi(2R_c)/n \sim n^{-1/2}$. We note that whereas Voronoi cells are always convex, the ‘curve’ connecting the first neighbors need not enclose a convex area; in each of the Figs. 5, 6, and 7 there are small but clearly distinguishable deviations from convexity.

Fig. 8 enlarges a detail of Fig. 7 and shows a collection of first-neighbor

cells. All first neighbors fully visible in the figure are four-sided except those marked A , B , D , E , which are five-sided, and the cell C , which is either five- or six-sided (this depends on how the two almost coinciding three-vertices are arranged at the point marked ‘2V’; a higher resolution is needed to decide this question). Fig. 8 illustrates that in the limit of large n four-sided first neighbors become dominant. In Ref. [4] it was argued that five-sided cells constitute a fraction only of order $n^{-1/2}$ of all first-neighbor cells, and that the probability of six- and higher-sided first-neighbors is of still higher order in $n^{-1/2}$. In Fig. 8 the cell marked P is a second neighbor to the central cell. The boundary separating it from the first neighbors has been shown as a heavy solid line on which we will further comment shortly.

4.2 Very large cells

Focusing now on very large n we show in Fig. 9 a central particle located in the origin and having 1536 neighbors. As before, the dots represent the particles. The inner contour, which is nearly indistinguishable from a circle of radius R_c , represents the boundary of the Voronoi cell of the central particle. The outer ‘curve’, which is also very close to circular but of radius $2R_c$, represents the alignment of the 1536 first-neighbor particles. Their high line density gives the impression of a continuous curve. Cell boundaries other than those of the central cell have not been drawn; they would totally blacken the empty annular region between the boundary of the central cell and its first-neighbor particles.

The boxed region in Fig. 9 is shown enlarged in Fig. 10, where we did draw all Voronoi cell boundaries. The extreme elongation of the first-neighbor cells is what first strikes the eye. The discrete structure of the ‘curve’ of first neighbors is also apparent now. The distances ℓ_m between successive first-neighbor particles along this curve are of order $n^{-1/2}$. More precisely, if we set $\ell_m = \lambda_m(4\pi/n)^{1/2}$, then the theory [1] implies that for $n \rightarrow \infty$ the λ_m are independent identically distributed random variables of probability law $\lambda_m \exp(-\lambda_m)$. Random deviations from a local straight line are too small to be discernible to the eye; they may be argued [26] to decrease as $n^{-3/2}$, which is also the order of magnitude of the systematic deviations due to the radius of curvature $2R_c$. The large cell and its environment are characterized, therefore, by four different length scales, each varying with its own power of n . They have been summarized in Table 4 below. One has to go to n values as high as we did in order for the separation of scales to become clearly visible.

Very large n is required also for still another feature to become apparent. In Fig. 10 the boundary between a second-neighbor cell and its adjacent first-neighbor cells is, by construction, composed of points equidistant to the second-neighbor particle and the almost continuous straight line of first--

Scale	Length
$n^{1/2}$	Cell radius
n^0	Typical interparticle distance outside the first neighbor circle
$n^{-1/2}$	Typical distance between successive first neighbor particles
$n^{-3/2}$	Random deviations of first neighbors from full alignment

Table 4: Four length scales characterizing the n -sided Voronoi cell in the large n limit; see Figs. 9 and 10.

neighbor particles. But such a boundary is a parabola. Hence, in the limit $n \rightarrow \infty$ the boundary separating the set of first from the set of second-neighbor cells is *piecewise parabolic*. Indeed, with this observation in mind one now recognizes the boundary segment of cell P in Fig. 8 (heavy solid line), and others in that same figure, as ‘incipient parabolic’. Such knowledge was at the basis of the theory of two-cell correlations exposed in Ref. [4]. There, laws discovered in the $n \rightarrow \infty$ limit were extrapolated backward and shown to be relevant for finite n . It was shown, in particular, that Aboav’s linear relationship [12, 2] between n and the total average sidedness nm_n of the neighbors of an n -sided cell cannot hold in Poisson-Voronoi diagrams. We expect that in the future the study of large cells will shed further light also on various issues relevant for the finite n behavior.

5 Summary and conclusion

In this paper we have developed a new Monte Carlo method for evaluating the sidedness probability p_n for arbitrary n . The method, which is constructed on the basis of an extension of earlier theory [3, 1], is not difficult to implement once one has available the rather complicated analytic expressions that intervene.

We have determined p_n as well as the first and second moments of the n dependent cell perimeter and cell area. Full agreement is obtained with earlier results for p_n due to Hayen and Quine [6], Calka [7], and Brakke [8], whose data extend up to $n = 16$. For $n \gtrsim 10$ we have reduced the error bars on p_n very considerably. In the range up to $n = 50$ we improved and corrected the p_n data due to Drouffe and Itzykson [9]. For $50 < n \leq 1600$ we obtained data in a range that had so far remained inaccessible. This enabled us to investigate the asymptotic large n behavior of p_n and of the perimeter and area moments. On the basis of our numerical results we conclude that they all have asymptotic series in entire powers of n^{-1} , possibly up to an overall prefactor $n^{\frac{1}{2}}$.

Exploiting our full control of the cell statistics we have exhibited occurrences of extremely rare many-sided cells in a typical environment of ordinary

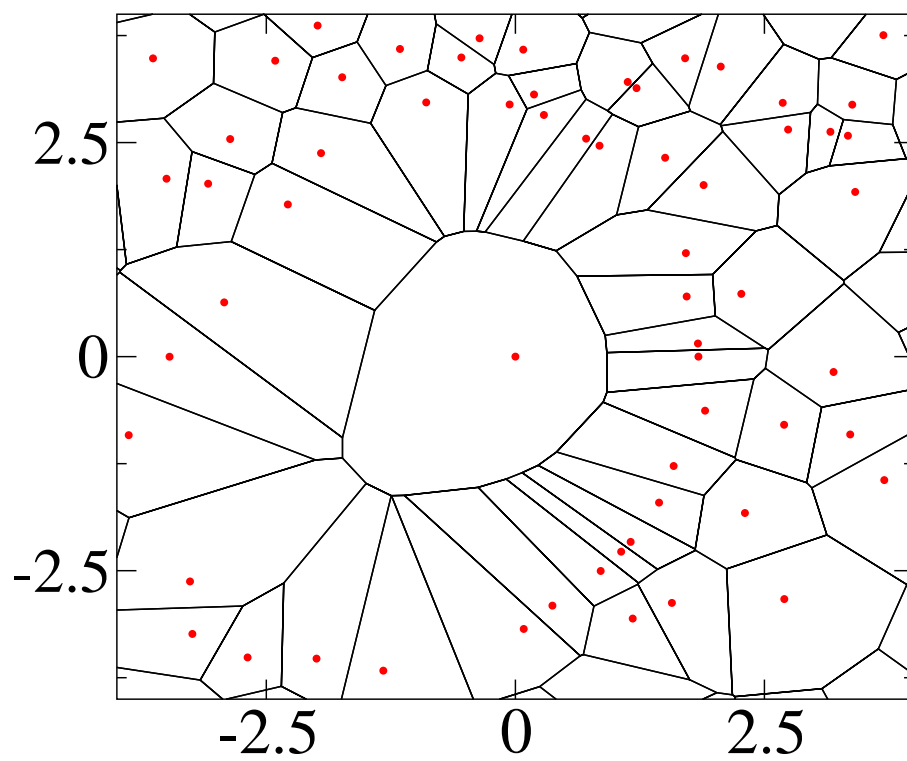


Figure 5: A typical Voronoi cell with $n = 24$ neighbors. The dots represent the particles.

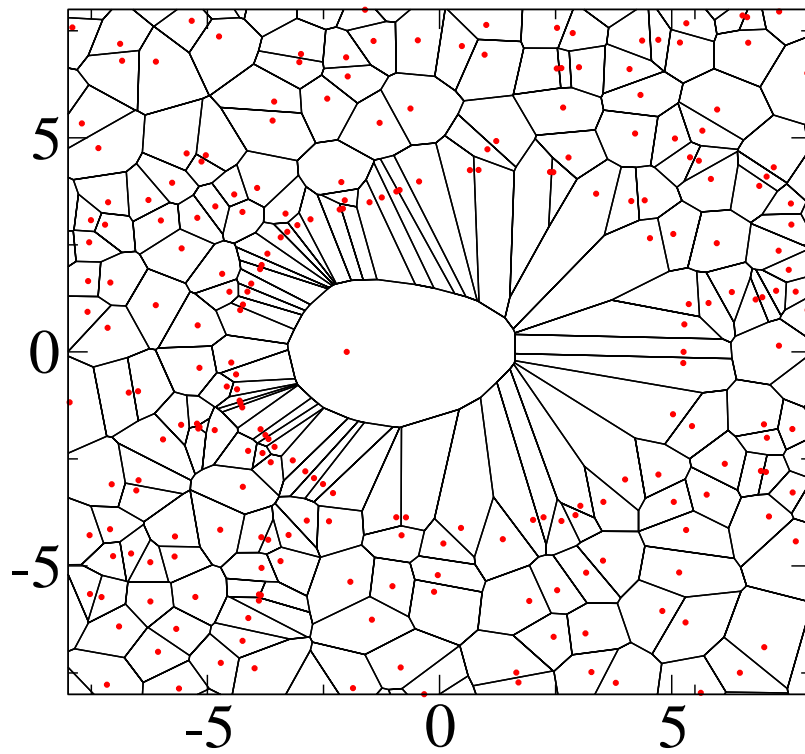


Figure 6: A typical Voronoi cell with $n = 48$ neighbors.

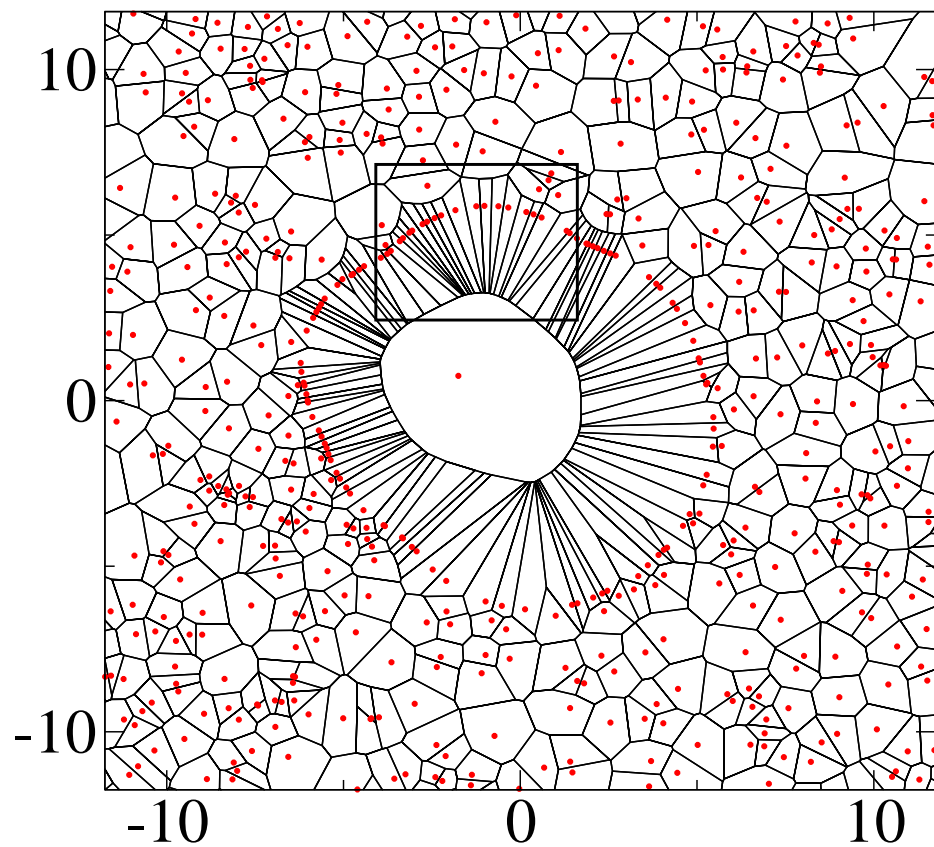


Figure 7: A typical Voronoi cell with $n = 96$ neighbors. The region inside the box is shown enlarged in Fig. 8.

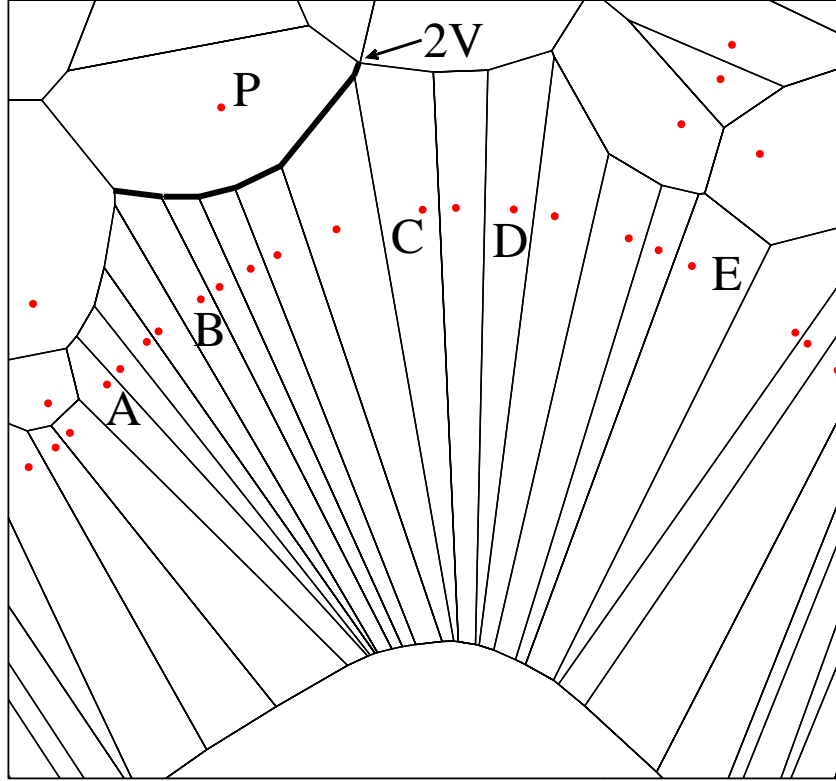


Figure 8: Enlargement of the box in Fig. 7 showing some of the strongly elongated first neighbors of the central cell. Among the first neighbors fully visible, cells A , B , C , D , and E have more than four sides. The arrow marked ‘ $2V$ ’ points to two three-vertices that coincide within the resolution of the figure. Cell P is a second neighbor whose boundary with the first neighbors (heavy lines) is an example of an ‘incipient parabola segment’ (see text).

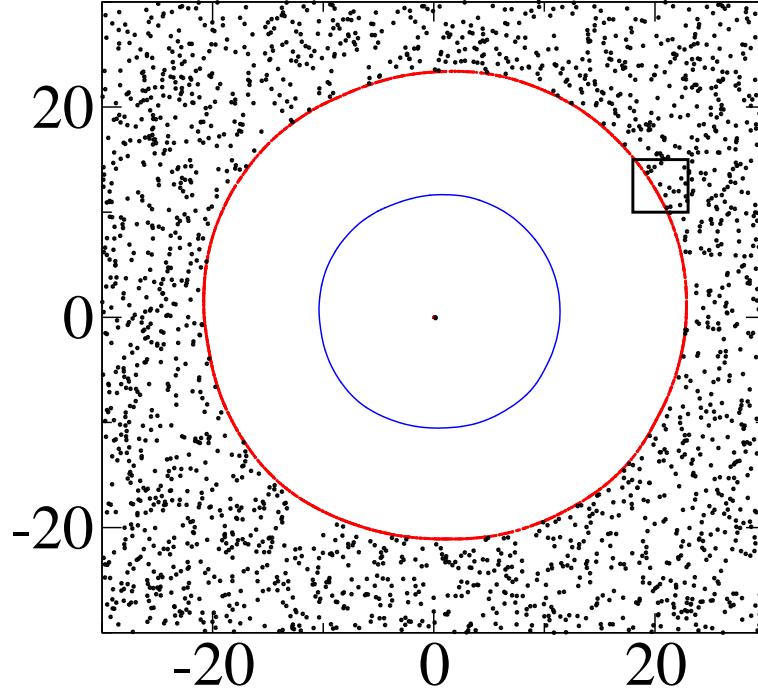


Figure 9: Approach to the infinite n limit. The origin is occupied by a particle whose Voronoi cell has $n = 1536$ sides. The almost circular inner curve is the cell boundary of the central cell. The other cells boundaries have not been drawn. The almost circular outer curve is made up of the 1536 first-neighbor particles. The region inside the box is shown enlarged in Fig. 10.

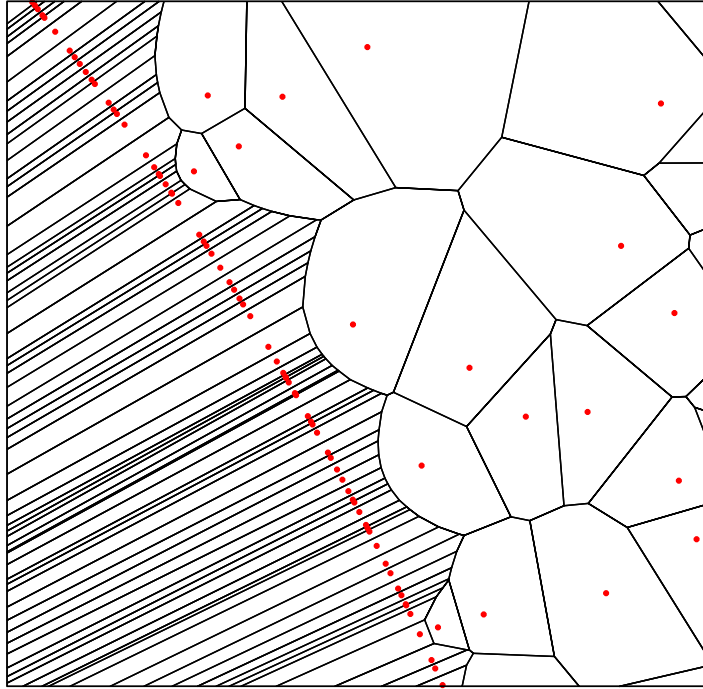


Figure 10: Enlargement of the box in Fig. 9, where now all cell boundaries have been drawn. The discrete structure of the outer ‘curve’ of Fig. 9 has become visible here.

cells. Their embedding involves four distinct length scales, varying with four different powers of n . This has confirmed, among several other things, the very elongated shape of the first-neighbor cells.

No particular effort was made to optimize the code. Our total investment of computer time on a recent model PC was limited to a few hundred hours and allowed us to obtain p_n to at least four or five significant decimals for the set of n values listed in the tables. We have also not attempted to provide any ‘best fits’ to the numerical curves, as we have no reason to believe that there exist simple analytic expressions that fit the data within our error bars over their full range.

The Monte Carlo work of this paper became possible only after initial analytic progress [3, 1]. We believe that it will in return spur further analytic investigation. One branch of study may concern the nature of the asymptotic expansions uncovered here. Another one may deal with correlations between a cell and its second, third, and higher topological neighbors, which are a recurrent theme in the theory and applications of Voronoi cells.

Acknowledgments

The author thanks Daniela de Oliveira Maionchi for providing him with the computer program that draws the Voronoi cells of a given set of particles. He thanks Pierre Calka for discussions and for indicating to him Ref. [6].

A Theory

We present here the extension of earlier work that opens the way to the numerical simulations of this work. We consider uniformly and independently distributed particles in the plane. Let a particle be placed in the origin and let n other particles occupy the positions $2\mathbf{R}_1, 2\mathbf{R}_2, \dots, 2\mathbf{R}_n$. The sidedness probability p_n of the cell containing the origin may then be written as a $2n$ -fold integral on the midpoint coordinates [9, 10, 14, 7],

$$p_n = \frac{1}{n!} \int d\mathbf{R}_1 \dots d\mathbf{R}_n \chi(\mathbf{R}_1, \dots, \mathbf{R}_n) e^{-\mathcal{A}(\mathbf{R}_1, \dots, \mathbf{R}_n)}. \quad (\text{A.1})$$

Here the indicator function χ is equal to unity (or to zero) on the domain of phase space where the perpendicular bisectors of the vectors $2\mathbf{R}_m$, for $m = 1, 2, \dots, n$, define an n -sided (or a fewer-sided) cell around the origin; and \mathcal{A} is the two-dimensional volume of the area that should be void of particles if this cell is not to be intersected by any of the bisectors of the position vectors of the remaining particles. Explicit expressions for \mathcal{A} and χ are given in Refs. [7, 1].

A.1 Starting point

After one integrates over a common radial scale, expression (A.1) takes the form [1] of an integral on the angle β_1 and on the sets of angles $\xi = \{\xi_m\}$ and $\eta = \{\eta_m\}$,

$$p_n = \frac{(n-1)!}{2n} \int_{-\pi/2}^{\pi/2} d\beta_1 \int d\xi d\eta \delta\left(\sum_{m=1}^n \xi_m - 2\pi\right) \delta\left(\sum_{m=1}^n \eta_m - 2\pi\right) \\ \times \frac{\delta(\beta_1 - \beta_*)}{G'(\xi, \eta; \beta_*)} \left[\prod_{m=1}^n \rho_m^2 T_m \right] [\pi(1 + n^{-1}V)]^{-n}, \quad (\text{A.2})$$

where G and β_* are as defined in the main text [Eqs. (2.2) and (2.1)] and the derivative $G' = dG/d\beta_1$ is given explicitly by (B.8) and (B.4) of Appendix B. The definitions of the new symbols occurring in (A.2) follow below.

First of all, the symbol $\int d\xi d\eta$ in (A.2) is shorthand for the nested integrations

$$\int d\xi d\eta = \int_0^{\pi/2+\beta_1} d\xi_1 \int_0^{\pi/2+\gamma_1} d\eta_1 \int_0^{\pi/2+\beta_2} d\xi_2 \dots \\ \dots \int_0^{\pi/2+\gamma_{n-1}} d\eta_{n-1} \int_0^{\pi/2+\beta_n} d\xi_n \int_0^{2\pi} d\eta_n. \quad (\text{A.3})$$

The notation is hybrid; the variables $\gamma_1, \beta_2, \gamma_3, \dots, \beta_n$ occurring here should be viewed as functions of ξ, η , and the ‘angle of rotation’ β_1 . They are given by

$$\beta_m = \beta_*(\xi, \eta) - \sum_{\ell=1}^{m-1} (\xi_\ell - \eta_\ell), \\ \gamma_m = -\beta_*(\xi, \eta) + \sum_{\ell=1}^{m-1} (\xi_\ell - \eta_\ell) + \xi_m, \quad m = 1, \dots, n, \quad (\text{A.4})$$

where $\sum_{\ell=1}^0$ denotes an empty sum. Next, the T_m and ρ_m are functions of the γ_m and β_m given by

$$T_m = \frac{\sin(\beta_m + \gamma_m)}{\cos^2 \beta_m}, \quad m = 1, \dots, n, \quad (\text{A.5})$$

$$\rho_m = \frac{\cos \gamma_m \cos \gamma_{m-1} \dots \cos \gamma_1}{\cos \beta_m \cos \beta_{m-1} \dots \cos \beta_1} \rho_n, \quad m = 1, \dots, n-1, \quad (\text{A.6})$$

and the condition

$$n^{-1} \sum_{m=1}^n \rho_m = 1. \quad (\text{A.7})$$

Finally V is given by

$$\begin{aligned}
V = & \frac{n}{4\pi} \sum_{m=1}^n \rho_m^2 \left[\tan \gamma_m - \gamma_m + \tan \beta_{m+1} - \beta_{m+1} \right. \\
& \left. + \gamma_m \tan^2 \gamma_m + \beta_{m+1} \tan^2 \beta_{m+1} \right] \\
& + \frac{n}{2\pi} \sum_{m=1}^n (\rho_m^2 - 1)(\gamma_m + \beta_{m+1}). \tag{A.8}
\end{aligned}$$

The factor n included in its definition makes that, typically, V is of order n^0 as $n \rightarrow \infty$. This completes the definition of the multiple integral (A.2) for p_n .

A.2 Transformations

We now depart from the development of Ref. [1] and transform expression (A.2) as follows. We integrate over β_1 and henceforth when writing β_1 it will be understood that it takes the value $\beta_1 = \beta_*(\xi, \eta)$. The integration requires that Eq. (2.1) have a solution. In Ref. [1] a unique solution was shown to exist perturbatively for large n ; in Appendix B of the present work we provide the demonstration for general n . We furthermore replace the upper integration limits of the integrals over the ξ_m and η_m by ∞ at the expense of introducing Heaviside theta functions. Using that $\xi_m - \beta_m = \gamma_m$ and $\eta_m - \gamma_m = \beta_{m+1}$ and introducing a factor $\theta(\frac{\pi}{2} - \beta_1)$, which may be done for free we find that Eq. (A.2) may be converted into

$$\begin{aligned}
p_n = & \frac{(n-1)!}{2n\pi^n} \int_0^\infty d\xi_1 \xi_1 \dots d\xi_n \xi_n \int_0^\infty d\eta_1 \dots d\eta_n \\
& \times \delta\left(\sum_{m=1}^n \xi_m - 2\pi\right) \delta\left(\sum_{m=1}^n \eta_m - 2\pi\right) \Theta e^{-V}, \tag{A.9}
\end{aligned}$$

in which

$$e^{-V} = G'(\xi, \eta; \beta_*)^{-1} \left[\prod_{m=1}^n \rho_m^2 T_m \xi_m^{-1} \right] (1 + n^{-1}V)^{-n} \tag{A.10}$$

and

$$\Theta = \prod_{m=1}^n \theta\left(\frac{\pi}{2} - \beta_m\right) \prod_{m=1}^n \theta\left(\frac{\pi}{2} - \gamma_m\right). \tag{A.11}$$

Expression (A.9) is more symmetric than (A.2)-(A.3). Its integrand is a function exclusively of the ξ_m and η_m . We have purposefully included extra weights ξ_m in the integrations in (A.9) and compensated for these by factors ξ_m^{-1} in the product on m in (A.10). In this way we obtain property that $T_m \xi_m$

remains finite when $\xi_m \rightarrow 0$, which was desirable analytically [3, 1] and is also necessary numerically.

The same quantity \mathbb{V} as defined in (A.10) was studied analytically in Refs. [3, 1], where it was shown that for $n \rightarrow \infty$ it remains, typically, of order n^0 .

One further rewriting is useful. We set

$$\xi_m = \alpha_{2m-1} + \alpha_{2m}, \quad m = 1, 2, \dots, n, \quad (\text{A.12})$$

and use that

$$\int_0^\infty d\alpha_{2m-1} d\alpha_{2m} f(\alpha_{2m-1} + \alpha_{2m}) = \int_0^\infty d\xi_m \xi_m f(\xi_m) \quad (\text{A.13})$$

for any function $f(\xi_m)$. This converts (A.9) into the final result

$$p_n = p_n^{(0)} \langle \Theta e^{-\mathbb{V}} \rangle, \quad (\text{A.14})$$

where for any function X of the angular variables the average $\langle X \rangle$ is defined by

$$\begin{aligned} \langle X \rangle &= \frac{1}{p_n^{(0)}} \int_0^\infty d\alpha_1 \dots d\alpha_{2n} \int_0^\infty d\eta_1 \dots d\eta_n \\ &\quad \times \delta\left(\sum_{m=1}^{2n} \alpha_m - 2\pi\right) \delta\left(\sum_{m=1}^n \eta_m - 2\pi\right) X. \end{aligned} \quad (\text{A.15})$$

The normalization factor $p_n^{(0)}$ that appears here is easily calculated as

$$\begin{aligned} p_n^{(0)} &= \frac{(n-1)!}{2n\pi^n} \left[\int_0^\infty d\alpha_1 \dots d\alpha_{2n} \delta\left(\sum_{m=1}^{2n} \alpha_m - 2\pi\right) \right] \\ &\quad \times \left[\int_0^\infty d\eta_1 \dots d\eta_n \delta\left(\sum_{m=1}^n \eta_m - 2\pi\right) \right] \\ &= \frac{(n-1)!}{2n\pi^n} \times \frac{(2\pi)^{2n-1}}{(2n-1)!} \times \frac{(2\pi)^{n-1}}{(n-1)!} \\ &= \frac{(8\pi^2)^n}{4\pi^2(2n)!}, \end{aligned} \quad (\text{A.16})$$

which is (1.2). This way of arriving at $p_n^{(0)}$ is slightly simpler than the original calculation of Ref. [1]. Expressions (A.14)-(A.15) are new and are at the basis of the Monte Carlo simulation of this work. The integrals in (A.15) directly suggest step (i) of the algorithm of subsection (2.3).

B The equation $G = 0$

We discuss here the function G defined by

$$e^{2\pi G} = \frac{\cos \gamma_1 \cos \gamma_2 \dots \cos \gamma_n}{\cos \beta_1 \cos \beta_2 \dots \cos \beta_n}. \quad (\text{B.1})$$

The transformation to angular variables in Appendix A led to Eq. (A.11), *i.e.* to the upper limits of integration $\beta_m, \gamma_m < \frac{\pi}{2}$. Since $\beta_m + \gamma_m = \xi_m$ and since $\xi_m > 0$, we have in fact that in the integral for p_n the angles β_m and γ_m are restricted by

$$-\frac{\pi}{2} < \beta_m, \gamma_m < \frac{\pi}{2}. \quad (\text{B.2})$$

Hence $G \rightarrow -\infty$ whenever any of the γ_m tends to $\pm\frac{\pi}{2}$, and $G \rightarrow \infty$ whenever any of the β_m tends to $\pm\frac{\pi}{2}$. We set now

$$\begin{aligned} \beta_m &= \tilde{\beta}_m + \beta_1, \\ \gamma_m &= \tilde{\gamma}_m - \beta_1, \quad m = 1, \dots, n, \end{aligned} \quad (\text{B.3})$$

where the $\tilde{\beta}_m$ and $\tilde{\gamma}_m$ are functions of the ξ_m and η_m that may be read off by a comparison of Eqs. (B.3) and (A.4),

$$\begin{aligned} \tilde{\beta}_m &= -\sum_{\ell=1}^{m-1} (\xi_\ell - \eta_\ell), \\ \tilde{\gamma}_m &= \sum_{\ell=1}^{m-1} (\xi_\ell - \eta_\ell) + \xi_m, \quad m = 1, \dots, n. \end{aligned} \quad (\text{B.4})$$

where again $\sum_{\ell=1}^0$ denotes the empty sum. Making all β_1 dependence explicit we get

$$e^{2\pi G} = \frac{\cos(\tilde{\gamma}_1 - \beta_1) \cos(\tilde{\gamma}_2 - \beta_1) \dots \cos(\tilde{\gamma}_n - \beta_1)}{\cos(\tilde{\beta}_1 + \beta_1) \cos(\tilde{\beta}_2 + \beta_1) \dots \cos(\tilde{\beta}_n + \beta_1)} \quad (\text{B.5})$$

which we wish to study as a function of the single variable β_1 , at fixed (ξ, η) . Expression (B.5) shows that $\exp(2\pi G)$ is positive on the interval

$$-\frac{\pi}{2} + \max_{1 \leq m \leq n} \tilde{\gamma}_m < \beta_1 < \frac{\pi}{2} - \max_{1 \leq m \leq n} \tilde{\beta}_m, \quad (\text{B.6})$$

provided this interval is not empty, that is, provided

$$\max_{1 \leq m \leq n} \tilde{\gamma}_m + \max_{1 \leq m \leq n} \tilde{\beta}_m < \pi. \quad (\text{B.7})$$

Because of the preceding discussion, G approaches $-\infty$ and ∞ as β_1 approaches the left and right hand end points of this interval, respectively. To

show that G is actually monotonous in β_1 on the interval (B.6), it suffices to analyze the derivative

$$\frac{dG}{d\beta_1} = \frac{1}{2\pi} \sum_{m=1}^n [\tan(\tilde{\gamma}_m - \beta_1) + \tan(\tilde{\beta}_m + \beta_1)]. \quad (\text{B.8})$$

Since $\tilde{\beta}_m + \tilde{\gamma}_m = \xi_m > 0$, it follows that there are three cases, namely (i) $\tilde{\beta}_m, \tilde{\gamma}_m > 0$, (ii) $\tilde{\beta}_m > 0, \tilde{\gamma}_m < 0$, and (iii) $\tilde{\beta}_m < 0, \tilde{\gamma}_m > 0$. By considering each of them separately one deduces that the summand in Eq. (B.8) is always positive. It follows that $dG/d\beta_1 > 0$ and hence that $G = 0$ has a unique solution $\beta_1 = \beta_*(\xi, \eta)$ in the interval (B.6).

Hence we have shown that the conditions $\xi_m, \eta_m > 0$ and $\beta_m, \gamma_m < \frac{\pi}{2}$ suffice for the equation $G = 0$ to have a unique solution β_* in the physical interval (B.6). This condition involves, however, the angles β_m and γ_m which are determined by the solution β_* . We would like to have a criterion for the existence of a solution in terms of the sole sets (ξ, η) given at the outset. By retracing the solution method, we see that it is valid for all (ξ, η) as long as the ‘physical’ interval (B.6) is not empty, that is, as long as Eq. (B.7) is satisfied. When made explicit with the aid of (B.4), Eq. (B.7) becomes condition (2.3) of the main text.

References

- [1] H.J. Hilhorst, *J. Stat. Mech.* P09005 (2005).
- [2] A. Okabe, B. Boots, K. Sugihara, and S.N. Chiu, *Spatial tessellations: concepts and applications of Voronoi diagrams*, second edition (John Wiley & Sons Ltd., Cichester, 2000).
- [3] H.J. Hilhorst, *J. Stat. Mech.* L02003 (2005).
- [4] H.J. Hilhorst, *J. Phys. A* **39** (2006) 7227.
- [5] J. L. Meijering, *Philips Research Reports* **8**, 270 (1953).
- [6] A. Hayen and M.P. Quine, *J. Statist. Comput. Simul.* **67**, 351 (2000).
- [7] P. Calka, *Adv. in Appl. Probab.* **35**, 863 (2003).
- [8] K.A. Brakke, unpublished.
Available on <http://www.susqu.edu/brakke/aux/downloads/200.pdf>.
- [9] J.M. Drouffe and C. Itzykson, *Nuclear Physics* **B235** [FS11], 45 (1984).

- [10] C. Itzykson and J.M. Drouffe, *Statistical field theory* (Cambridge University Press, Cambridge, 1989), Vol. 2, chapter 11.
- [11] G. Le Caër and R. Delannay, *J. Phys. A* **26**, 3931 (1993).
- [12] D.A. Aboav, *Metallography* **3**, 383 (1970).
- [13] Its analytic expression is $C = \prod_{q=1}^{\infty} (1 - q^{-2} + 4q^{-4})^{-1}$.
- [14] P. Calka, *Adv. in Appl. Probab.* **35**, 551 (2003).
- [15] The $\bar{\Psi}_m$ are equal to the angles Ψ_m of Fig. 1 up to a common additive constant which drops out of Eq. (2.4). An analogous remark applies to the $\bar{\Phi}_m$.
- [16] A factor 4λ instead of λ appears because the particle positions were defined as $2\mathbf{R}_m$ instead of \mathbf{R}_m .
- [17] For a figure comparing their data to our asymptotic result we refer to Ref. [3].
- [18] S. R. Finch, unpublished.
Available on <http://algo.inria.fr/csolve/vi.pdf>. Addendum to *Mathematical Constants*, Encyclopedia of Mathematics and its Applications 94, Cambridge University Press (2003).
- [19] F.T. Lewis, *Anatomical Records* **38**, 341 (1928); **47**, 59 (1930); **50**, 235 (1931).
- [20] R.E. Miles and R.J. Maillardet, *J. Appl. Probab. A* **19**, 97 (1982).
- [21] K.B. Lauritsen, C. Moukarzel, and H.J. Herrmann, *J. Phys. I France* **3**, 1941 (1993).
- [22] The approach of a Voronoi cell to a disk has been rigorously proved [23, 24, 25] under the condition of the cell becoming large (*e.g.*, by letting its area tend to infinity), rather than many-sided ($n \rightarrow \infty$). The two conditions lead to distinctly different statistical ensembles.
- [23] P. Calka, *Adv. in Appl. Probab.* **34**, 702 (2002).
- [24] D. Hug, M. Reitzner, and R. Schneider, *Adv. in Appl. Probab.* **36**, 667 (2004).
- [25] P. Calka and T. Schreiber, *to appear in Ann. Probab.*
- [26] H.J. Hilhorst, unpublished.